

This item is likely protected under Title 17 of the U.S. Copyright Law. Unless on a Creative Commons license, for uses protected by Copyright Law, contact the copyright holder or the author.

Access to this work was provided by the University of Maryland, Baltimore County (UMBC) ScholarWorks@UMBC digital repository on the Maryland Shared Open Access (MD-SOAR) platform.

Please provide feedback

Please support the ScholarWorks@UMBC repository by emailing scholarworks-group@umbc.edu and telling us what having access to this work means to you and why it's important to you. Thank you.

PULSE PHASE-RESOLVED ANALYSIS OF THE HIGH-MASS X-RAY BINARY CENTAURUS X-3 OVER TWO BINARY ORBITS

SLAWOMIR SUCHY,¹ KATJA POTTSCHMIDT,^{1,2,3} JÖRN WILMS,⁴ INGO KREYKENBOHM,^{5,6} GABRIELE SCHÖNHERR,⁷
 PETER KRETSCHMAR,⁸ VANESSA MCBRIDE,⁹ ISABEL CABALLERO,⁵
 RICHARD E. ROTHSCILD,¹ AND VICTORIA GRINBERG¹⁰

Received 2007 August 29; accepted 2007 November 17

ABSTRACT

We present a detailed analysis of observations of the high-mass X-ray binary Cen X-3, spanning two consecutive binary orbits performed with the *RXTE* satellite in early March 1997. During this time Cen X-3 had a luminosity of $L_{2-10\text{ keV}} \sim (4-5) \times 10^{37} \text{ ergs s}^{-1}$ and a pulse period of 4.814 s. The PCA and HEXTE light curves both show a clear reduction in count rate after midorbit for both binary revolutions. We therefore analyze two broadband spectra for each orbit, before and after midorbit. Consistent with earlier observations, these four joint PCA and HEXTE spectra can be well described using a phenomenological pulsar continuum model, including an iron emission line and a cyclotron resonance-scattering feature. While no strong spectral variations were detected, the second half of orbit 2 shows a tendency toward being softer and more strongly absorbed. In order to follow the orbital phase-dependent evolution of the spectrum in greater detail, we model spectra for shorter exposures, confirming that most spectral parameters show either a gradual or sudden change for the second half of the second orbit. A comparison with a simple wind model indicates the existence of an accretion wake in this system. We also present and discuss high-resolution pulse profiles for several different energy bands, as well as their hardness ratios. PCA and HEXTE spectra were created for 24 phase bins and fitted using the same model as in the phase-averaged case. Systematic pulse phase-dependent variations of several continuum and cyclotron line parameters were detected, most notably a significant increase of the cyclotron line energy during the early rise of the main peak, followed by a gradual decrease. We show that applying a simple dipole model for the magnetic field is not sufficient to describe our data.

Subject headings: pulsars: individual (Centarus X-3) — stars: magnetic fields — X-rays: binaries — X-rays: stars

Online material: color figures

1. INTRODUCTION

The pulsar nature of the accreting high-mass X-ray binary (HMXB) Centaurus X-3 was discovered by *Uhuru* (Schreier et al. 1972; Giacconi et al. 1971), measuring a spin period of ~ 4.8 s and an orbital period of ~ 2.1 days. The binary system consists of a neutron star with a mass of $1.21 \pm 0.21 M_{\odot}$ accompanied by an O 6–8 III supergiant star with a mass of $20.5 \pm 0.7 M_{\odot}$ (Hutchings et al. 1979; Ash et al. 1999). The distance of the binary system has been estimated to be roughly 8 kpc, with a lower limit of 6.2 kpc (Krzeminski 1974) and an eccentricity

of ≤ 0.0016 (Bildsten et al. 1997). Day & Tennant (1991) used dust-scattering measurements to derive a distance of 5.4 ± 0.3 kpc, a result only marginally consistent with Krzeminski (1974) within given uncertainties. In order to allow for easier comparison with earlier publications, we adopt the widely used distance of 8 kpc. HMXBs generally show a strong stellar wind, which can supply a continuous tidal stream to the compact object when the companion star is close to filling its Roche lobe (Petterson 1978; Stevens 1988; Blondin et al. 1991). Day et al. (1993) discussed that in a system like Cen X-3 an X-ray-excited wind would be sufficient as a possible mechanism for mass transfer able to sustain a constant mass flux. A system with a combined mass transfer mechanism is, e.g., GX 301–2 (Leahy 2002; Leahy & Kostka 2008), where the folded *Rossi X-Ray Timing Explorer* (*RXTE*) ASM light curve was best modeled by a stellar wind with an additional gas stream as described by Stevens (1988). In addition, evidence for an accretion disk in Cen X-3 can be found: Tjemkes et al. (1986) compared the observed light curve of Cen X-3 with modeled binary light curves and achieved best results when including an accretion disk. The observed overall spin-up trend of 1.135 ms yr^{-1} with fluctuations on timescales of a few years (Tsunemi et al. 1996) also indicates the presence of an accretion disk, attributed to Roche lobe overflow. A realistic picture of the mass transfer mechanism in Cen X-3 would therefore be a combination of disk accretion and an excited stellar wind, as proposed by Petterson (1978).

An absorption feature in the X-ray spectrum at ~ 30 keV, interpreted as a cyclotron resonance-scattering feature (CRSF), also known as a cyclotron line, was first observed in Cen X-3 with *Ginga* by Nagase et al. 1992. *BeppoSAX* and *RXTE* HEXTE

¹ University of California, San Diego, Center for Astrophysics and Space Sciences, 9500 Gilman Drive, La Jolla, CA 92093-0424; ssuchy@ucsd.edu, kpottschmidt@ucsd.edu, rrothschild@ucsd.edu.

² Department of Physics, University of Maryland Baltimore County, 1000 Hilltop Circle, Baltimore, MD 21250.

³ NASA Goddard Space Flight Center, Astrophysics Science Division, Code 661, Greenbelt, MD 20771; katja@milkyway.gsfc.nasa.gov.

⁴ Dr. Karl-Remeis-Sternwarte, Astronomisches Institut, Sternwartstrasse 7, 96049 Bamberg, Germany; joern.wilms@sternwarte.uni-erlangen.de.

⁵ Institut für Astronomie und Astrophysik, Abt. Astronomie, Sand 1, 72076 Tübingen, Germany; kreyken@astro.uni-tuebingen.de, isabel@astro.uni-tuebingen.de.

⁶ *INTEGRAL* Science Data Centre, Chemin d’Écogia 16, 1290 Versoix, Switzerland; ingo.kreykenbohm@obs.unige.ch.

⁷ Astrophysikalisches Institut Potsdam, An der Sternwarte 16, 14482 Potsdam, Germany; gschoenherr@aip.de.

⁸ European Space Agency, European Space Astronomy Centre, P.O. Box 78, 28691 Villanueva de la Cañada, Madrid, Spain; peter.kretschmar@esa.int.

⁹ School of Physics and Astronomy, Southampton University, Southampton, SO17 1BJ, UK; vanessa@astro.soton.ac.uk.

¹⁰ Fakultät für Physik, Ludwig-Maximilians-Universität München, Schellingstrasse 4, 80799 München, Germany; victoria.grinberg@physik.lmu.de.

confirmed this feature at 28 and 30 keV, respectively (Santangelo et al. 1998; Heindl & Chakrabarty 1999). It is assumed to be the fundamental line, and so far no higher line harmonics have been observed for this source. CRSFs are generated due to the interaction of photons with electrons that are quantized in Landau levels, the discrete energy states populated by electrons in strong magnetic fields. Photons of energies corresponding to the separation of the Landau levels are absorbed and reemitted by the electrons. The net effect is that photons from the accretion column above the magnetic poles that have energies near the CRSF centroid energy are scattered out of the line of sight and/or redistributed in energy. These features can be used to measure directly the magnetic field strength in the line-forming region, since the fundamental cyclotron line energy is given by

$$E_{\text{cyc}} = \frac{1}{1+z} \frac{\hbar e B}{m_e} = \frac{11.6 \text{ keV}}{1+z} B_{12}, \quad (1)$$

where B_{12} is the magnetic field strength near the neutron star surface, in units of 10^{12} G, and z is the gravitational redshift (Canuto & Ventura 1977). Assuming a typical neutron star mass of $1.4 M_{\odot}$ and a neutron star radius of 10 km gives $z = 0.3$. Cen X-3's cyclotron line at ~ 30 keV then corresponds to a magnetic field of $\sim 3.4 \times 10^{12}$ G.

Kohmura et al. (2001) analyzed the PCA data of this observation in the energy band 2–13 keV, which has a high time resolution of 15.625 ms. They saw a delay in the time variability of the iron *K* band by 0.39 ± 0.10 ms and concluded that these photons were reprocessed away from the neutron star (NS) and are probably part of the matter accreting onto the NS. A preliminary analysis by Heindl & Chakrabarty (1999) of the HEXTE data presented in this work concentrated on basic pulse phase-resolved spectroscopy, dividing the pulse profile into four broad phase bins, and provided a first indication of a possible increase of the cyclotron line energy during the rise of the main pulse. Systematic variations of the CRSF centroid energy over pulse phase have also been observed in other sources, e.g., Her X-1 (Soong et al. 1990; Gruber et al. 2001), Vela X-1 (La Barbera et al. 2003; Kreykenbohm et al. 2002), 4U 0352+309 (Coburn et al. 2001), 4U 1538–52 (Clark et al. 1990), and GX 301–2 (Kreykenbohm et al. 2004). The origin of these changes is not yet well understood. Straightforward mechanisms such as the angular dependence of relativistic corrections on the cyclotron energy may not be sufficient to explain the observed variations. Higher harmonics rarely, if ever, are integral multiples of the fundamental line energy. In some sources this can be explained by invoking the proper nonintegral line spacing expected from the relativistic cross section (e.g., Pottschmidt et al. 2005). However, more complicated mechanisms, such as a *B*-field gradient at the magnetic pole, have also been invoked (Nishimura 2005). In addition, a correlation between CRSF energy and luminosity can be observed in several sources (e.g., Mihara 1995; Mowlavi et al. 2006; La Barbera et al. 2005; Staubert et al. 2007; Nakajima et al. 2006).

In the following, we further characterize the phase dependence of the line parameters in Cen X-3 using the exceptionally long (spanning ~ 4 days, i.e., two binary revolutions) *RXTE* observation of the source in 1997. Burderi et al. (2000, hereafter B00) observed Cen X-3 simultaneously with *BeppoSAX*, overlapping 11 hr of *RXTE* observations during the first binary orbit. We compare our results with B00 whenever possible.

We use combined PCA and HEXTE data for the analysis, which allows us to constrain the continuum shape of the spec-

trum and the CRSF parameters much more strongly than with HEXTE alone. We compare our analysis with other cyclotron line sources and apply a newly developed physical model for the CRSF to the data. For the analysis over the orbit, we compare with a simplified wind model to discuss the evolution of N_{H} through the observation.

The remainder of this paper is organized as follows: basic observation parameters, as well as the data reduction, are described in § 2. In § 3 we describe the PCA and HEXTE light curves observed over the two binary orbits. Phase-averaged spectra for the first and second halves of each orbit and their best-fit models are presented in § 4, as well as the temporal evolution of the spectral parameters, with a resolution of roughly one *RXTE* orbit throughout the two Cen X-3 binary orbits. Section 5 is dedicated to the pulse phase-resolved analysis, including the presentation of pulse profiles in multiple energy bands and modeling of phase-resolved spectra. The results are discussed in § 6.

2. OBSERVATION AND DATA REDUCTION

RXTE observed Cen X-3 with the Proportional Counter Array (PCA; Jahoda et al. 2006) and the High Energy X-Ray Timing Experiment (HEXTE; Rothschild et al. 1998) between 1997 February 28 and March 3. The observation, proposal ID P20104, covered two consecutive binary orbits between eclipses, excluding the time of eclipse between orbits. The total exposure time of 310 ks was split into 12 shorter data sets (ObsIDs) of ~ 8 hr each.

The PCA consists of five Proportional Counter Units (PCUs) covering a nominal energy range from 2 to 60 keV. For $\sim 90\%$ of the time, all PCUs were collecting data during the observation, with PCU 3 being turned off during the remaining time. The PCA background was modeled using the Sky-VLE model. The HEXTE instrument consists of two independent clusters, each containing four NaI(Tl)/CsI(Na) phoswich scintillation counters, covering an energy range from 15 to 250 keV. Each cluster pointed alternately at the source and at the background, switching every 16 s. At any given time, one of the clusters was on-source.

The data were reduced using HEASOFT version 6.0.6., applying standard extraction criteria: a pointing offset of $<0.01^\circ$ from the nominal source position, an exclusion time for the South Atlantic Anomaly (SAA) of 30 minutes, and a source elevation of $>10^\circ$. We imposed a maximum electron ratio of 0.15 in order to filter for background flares, taking into account a slightly elevated electron ratio level due to the influence of the bright target source. Depending on the analysis method, further grouping and filtering of the resulting good time intervals (GTIs) were applied in order to derive the PCA and HEXTE light curves and spectra. Details are described below, including the respective choices of data modes and binning options. All HEXTE data products were dead-time corrected using the HEASOFT tool *hxtdead*. Since precise absolute flux measurements are beyond the scope of this paper, correction for the PCA dead time of a few percent has not been carried out. Systematic uncertainties of 0.5% were included in the PCA spectral data. All high time resolution products were converted to the frame of reference at barycenter. The orbital ephemeris presented by Bildsten et al. (1997) was adopted for the binary star correction. For spectral modeling we used XSPEC version 11.3.2p (Arnaud 1996).

3. BROADBAND ORBITAL LIGHT CURVE

We extracted PCA and HEXTE light curves for all available ObsIDs. For the PCA, standard2f mode data were used, selecting the well-calibrated energy range from 3 to 17 keV and the highest

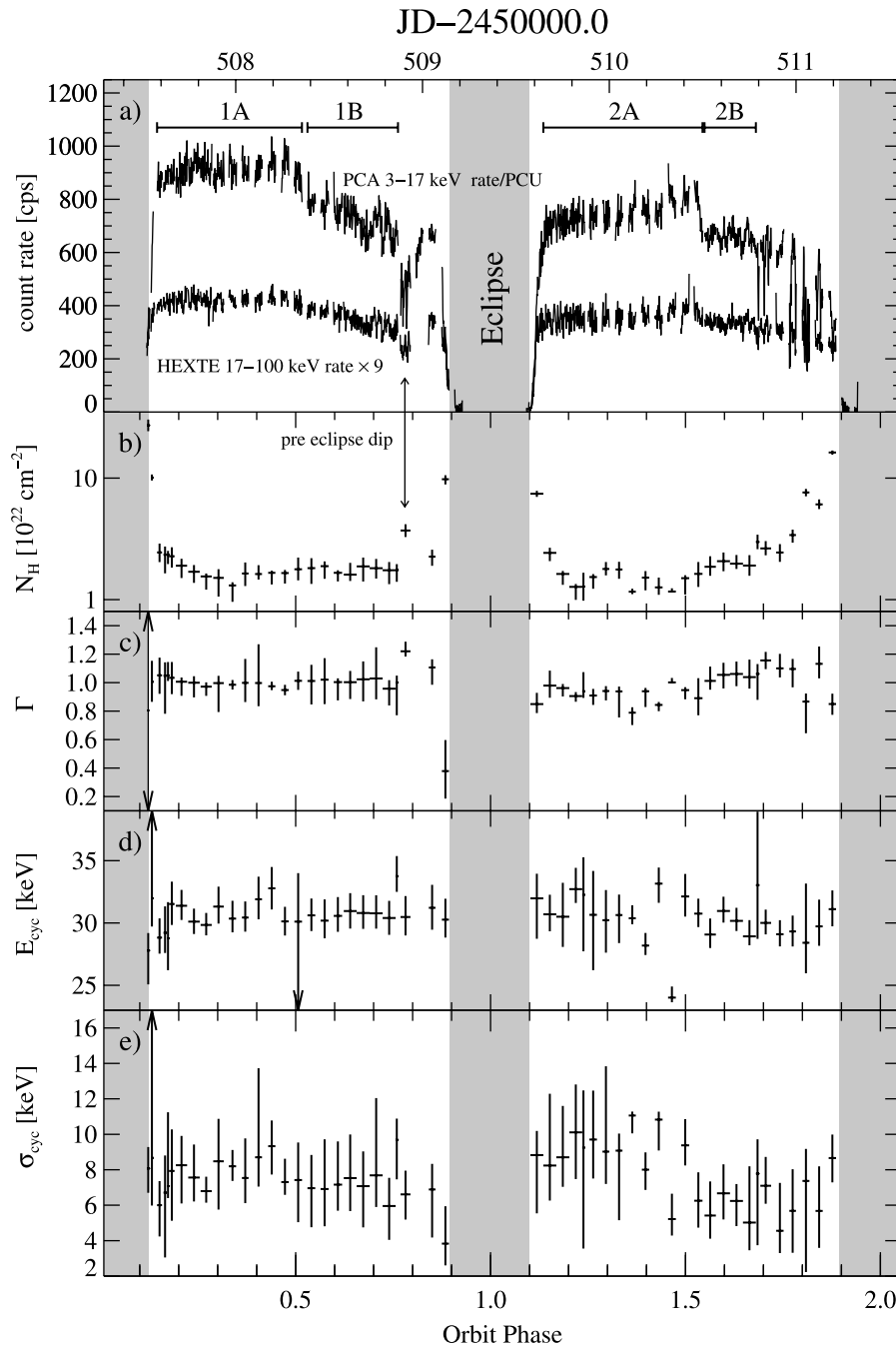


FIG. 1.—(a) Background-subtracted 3–17 keV PCA (top) and 17–100 keV HEXTE (bottom) light curves (bin time 128 s). The shaded region indicates the eclipse of the compact object. Error bars are not plotted, but are smaller than any visible variations. Horizontal lines above the data indicate the time intervals used for creating the time-averaged spectra analyzed in § 4.1. (b)–(e) Evolution of selected spectral parameters over two binary orbits. See text for model details. While the spectrum is stable—away from enhanced (pre)eclipse N_H —over the first orbit, the behavior changes significantly after the midorbit break of the second orbit. Data points from spectral analysis during eclipse are ignored. [See the electronic edition of the Journal for a color version of this figure.]

possible time resolution for this data mode of 16 s. Corresponding background model light curves were created. In the case of HEXTE, we use science event mode data from 17 to 100 keV, with the source not being significantly detected at higher energies. Since the HEXTE source and background measurements for each cluster are performed quasi-simultaneously due to the 16 s rocking cycle, the high time resolution background for HEXTE light curves with less than 16 s time resolution is based on interpolating the measured background rates. For each 1 s time-resolved data bin in a 16 s segment, we performed a linear interpolation of the background, using the neighboring 16 s

background pointings.¹¹ As HEXTEs cluster B has only three fully functional detectors, the count rate for this cluster was normalized to cluster A.

Figure 1a shows the background-subtracted PCA and HEXTE light curves (both rebinned to a resolution of 128 s for display purposes). The PCA light curve has been normalized to one PCU and the HEXTE light curve consists of the summed contributions

¹¹ More precisely, the background is measured during 12 s, preceded and followed by 2 s during which the cluster is moving between on- and off-source (Rothschild et al. 1998).

TABLE 1
BEST-FIT PARAMETERS FOR PHASE-AVERAGED SPECTRA OVER FIRST AND SECOND HALVES OF EACH BINARY ORBIT

Parameter	1A	1B	2A	2B
N_{H} (10^{22} cm^{-2})	$1.6^{+0.4}_{-0.2}$	$1.8^{+0.5}_{-0.5}$	$1.3^{+0.4}_{-0.2}$	$2.4^{+0.5}_{-0.4}$
E_{cut} (keV)	$11.1^{+1.5}_{-2.3}$	$4.8^{+9.7}_{-4.8}$	$7.7^{+4.0}_{-2.5}$	$20.9^{+6.6}_{-7.1}$
E_{fold} (keV)	$7.2^{+0.2}_{-0.3}$	$7.7^{+0.8}_{-0.5}$	$7.2^{+0.1}_{-0.4}$	$6.6^{+1.0}_{-2.3}$
E_{cyc} (keV)	$30.7^{+0.5}_{-0.4}$	$31.2^{+0.7}_{-0.7}$	$31.5^{+0.6}_{-0.5}$	$30.3^{+0.7}_{-0.6}$
σ_{cyc} (keV)	$6.4^{+1.0}_{-0.8}$	$4.3^{+2.8}_{-1.6}$	$6.3^{+0.9}_{-0.5}$	$7.3^{+1.4}_{-1.6}$
τ_{cyc}	$0.67^{+0.17}_{-0.07}$	$0.48^{+0.27}_{-0.09}$	$0.61^{+0.09}_{-0.06}$	$0.97^{+1.52}_{-0.34}$
Γ	$0.92^{+0.06}_{-0.04}$	$0.88^{+0.20}_{-0.15}$	$0.76^{+0.05}_{-0.06}$	$1.16^{+0.17}_{-0.09}$
A_{pl} (photons $\text{cm}^{-2} \text{ s}^{-1}$)	$0.70^{+0.07}_{-0.05}$	$0.75^{+0.33}_{-0.18}$	$0.52^{+0.12}_{-0.08}$	$0.58^{+0.10}_{-0.06}$
E_{Fe} (keV)	$6.60^{+0.06}_{-0.05}$	$6.57^{+0.05}_{-0.05}$	$6.61^{+0.06}_{-0.05}$	$6.55^{+0.06}_{-0.06}$
σ_{Fe} (keV)	$0.13^{+0.18}_{-0.13}$	$0.22^{+0.17}_{-0.22}$	$0.09^{+0.21}_{-0.09}$	$0.27^{+0.15}_{-0.26}$
A_{Fe} (10^{-2} photons $\text{cm}^{-2} \text{ s}^{-1}$)	$1.40^{+0.26}_{-0.21}$	$1.91^{+1.22}_{-0.34}$	$1.33^{+0.36}_{-0.26}$	$0.94^{+0.18}_{-0.16}$
$E_{13 \text{ keV}}$ (keV)	$13.3^{+0.2}_{-0.2}$	$13.6^{+0.5}_{-0.4}$	$13.2^{+0.3}_{-0.7}$	$13.0^{+0.4}_{-0.7}$
$\sigma_{13 \text{ keV}}$ (keV)	$2.8^{+0.4}_{-0.3}$	$4.0^{+1.0}_{-1.1}$	$3.4^{+0.4}_{-1.3}$	$3.2^{+0.8}_{-0.6}$
$A_{13 \text{ keV}}$ (10^{-2} photons $\text{cm}^{-2} \text{ s}^{-1}$)	$5.2^{+4.4}_{-1.6}$	$23.0^{+35.0}_{-14.0}$	$7.0^{+5.3}_{-3.8}$	$3.1^{+5.3}_{-1.3}$
χ^2_{HEXTE}	$0.857^{+0.003}_{-0.003}$	$0.856^{+0.003}_{-0.003}$	$0.854^{+0.003}_{-0.003}$	$0.860^{+0.004}_{-0.004}$
$L_{2-10 \text{ keV}}$ (10^{37} ergs s^{-1})	$5.4^{+0.4}_{-0.5}$	$4.4^{+1.2}_{-1.1}$	$4.3^{+0.8}_{-0.3}$	$4.0^{+0.6}_{-1.0}$
$\chi^2_{\text{red}}/\text{dof}$	1.13/83	0.71/83	0.86/83	0.77/83

NOTES.—The data sets 1A–2B are defined in Fig. 1. Parameters listed are the hydrogen column density N_{H} ; the Fermi-Dirac cutoff and folding energies E_{cut} and E_{fold} ; the CRSF energy E_{cyc} , width σ_{cyc} , and depth τ_{cyc} ; the power-law index Γ and strength A_{pl} ; the Fe K emission-line energy E_{Fe} , width σ_{Fe} , and strength A_{Fe} ; and the 13 keV emission feature energy $E_{13 \text{ keV}}$, width $\sigma_{13 \text{ keV}}$, and strength $A_{13 \text{ keV}}$. Uncertainties are quoted at the 90% confidence level assuming independent parameters (see text for existing correlations). The flux normalization of the HEXTE instrument with respect to the PCA, χ^2_{HEXTE} , and the luminosity in the 2–10 keV energy range derived from the PCA, $L_{2-10 \text{ keV}}$, are also given.

of both clusters and has been multiplied by a factor of 9 for display purposes. The same general features are visible above and below 17 keV, indicating the absence of extreme spectral variability over the binary orbit. For orbital phase $\phi_{\text{orb}} \gtrsim 0.5$, both orbits show a clear drop in the count rates. In addition, the source was fainter overall during the second orbit, with the brighter first half of orbit 2 approximately at the same level as the less bright second half of orbit 1. The eclipse covers $\sim 20\%$ of the orbital period. Preeclipse dips can be observed in both orbits. Takeshima et al. (1991) and Nagase et al. (1992) also observed a drop in luminosity for the second part of the orbit, calling it a “preeclipse dip.” In our case, we distinguish between before and after mid-orbit breaks and use the term “preeclipse dip” for relatively short count rate drops, slightly longer than one satellite orbit.

In the first orbit, one single preeclipse dip is visible around $\phi_{\text{orb}} = 0.75$ (JD 2,450,508.4), where the PCA rate drops by a factor of 2. Unfortunately, no HEXTE data are available in the archive for the egress of this preeclipse, because the instrument was not turned on (PCA data are available). In the second orbit, dipping activity starts around the same ϕ_{orb} (JD 2,450,510.8); however, all preeclipse dips are partially obscured by data gaps due to SAA passages and earth occultations, so that no detailed analysis is possible.

Based on modeling the averaged spectrum for the first part of orbit 1 (1A in Fig. 1 and Table 1), we find a 2–10 keV unabsorbed flux of $7.0^{+0.5}_{-0.7} \times 10^{-9}$ ergs $\text{cm}^{-2} \text{ s}^{-1}$ with the PCA. Taking the dead-time influence into account increases the measured flux by a few percent. The *BeppoSAX* observation analyzed by B00 was performed between 1997 February 27, 19:45 and February 28, 11:00 (UT) and thus overlaps with parts of data set 1A of the *RXTE* observation. B00 find a somewhat lower post-eclipse egress 2–10 keV flux of 5.7×10^{-9} ergs $\text{cm}^{-2} \text{ s}^{-1}$. The 18% discrepancy in flux is not surprising, due to the uncertainty in the cross-calibration between the PCA and the *BeppoSAX*. We point out that the fluxes derived from the HEXTE instrument are 14% lower than those derived with the PCA (see χ^2_{HEXTE} in Table 1) and thereby agree much better with *BeppoSAX*. Based

on the PCA flux measurement, we derived a 2–10 keV luminosity of $5.4^{+0.4}_{-0.5} \times 10^{37}$ ergs s^{-1} , applying a distance of 8 kpc (B00; 4.4×10^{37} ergs s^{-1}). The fainter second orbit shows a 2–10 keV flux of $5.6^{+1.0}_{-0.4} \times 10^{-9}$ ergs $\text{cm}^{-2} \text{ s}^{-1}$ during its first half, corresponding to a luminosity of $4.3^{+0.8}_{-0.3} \times 10^{37}$ ergs s^{-1} . The luminosities after the mid-orbit drop are $4.4^{+1.2}_{-1.1} \times 10^{37}$ and $4.0^{+0.6}_{-1.0} \times 10^{37}$ ergs s^{-1} for orbit 1 and 2, respectively; i.e., the relative flux change in the second orbit is a factor of 2 smaller than in the first orbit.

4. PHASE-AVERAGED SPECTROSCOPY

4.1. Time-averaged Spectral Parameters

For each available ObsID, standard2f mode PCA spectra and standard science event mode HEXTE spectra were extracted, including the corresponding background spectra. All spectra within one of the four time intervals indicated in Figure 1a were added. The resulting time-averaged spectra are count rate selected in the sense that they are characterized by episodes of different average count rate levels within a given binary orbit; i.e., for each of the two orbits, the first interval spans the bright phase up to the mid-orbit break, while the second interval spans the time up to the onset of preeclipse dipping. Time-averaged broadband source spectra were modeled by taking background-subtracted PCA spectra from 3 to 23 keV and background-subtracted HEXTE spectra from 17 to 100 keV into account and rebinning data above 60 keV by a factor of 5. As the CRSF centroid energy is at ~ 30 keV and a contamination of our data due to the xenon K edge at 33 keV would be possible, we decided not to increase the PCA range up to 60 keV, as described by Rothschild et al. (2006, Appendix B).

The basic continuum we use throughout the paper is an absorbed power law with index Γ , modified by a Fermi-Dirac cutoff characterized by cutoff and folding energies E_{cut} and E_{fold} (local XSPEC model *fdcut*; Tanaka 1986), respectively,

$$F(E) = AE^{-\Gamma} \frac{1}{1 + e^{(E-E_{\text{cut}})/E_{\text{fold}}}}, \quad (2)$$

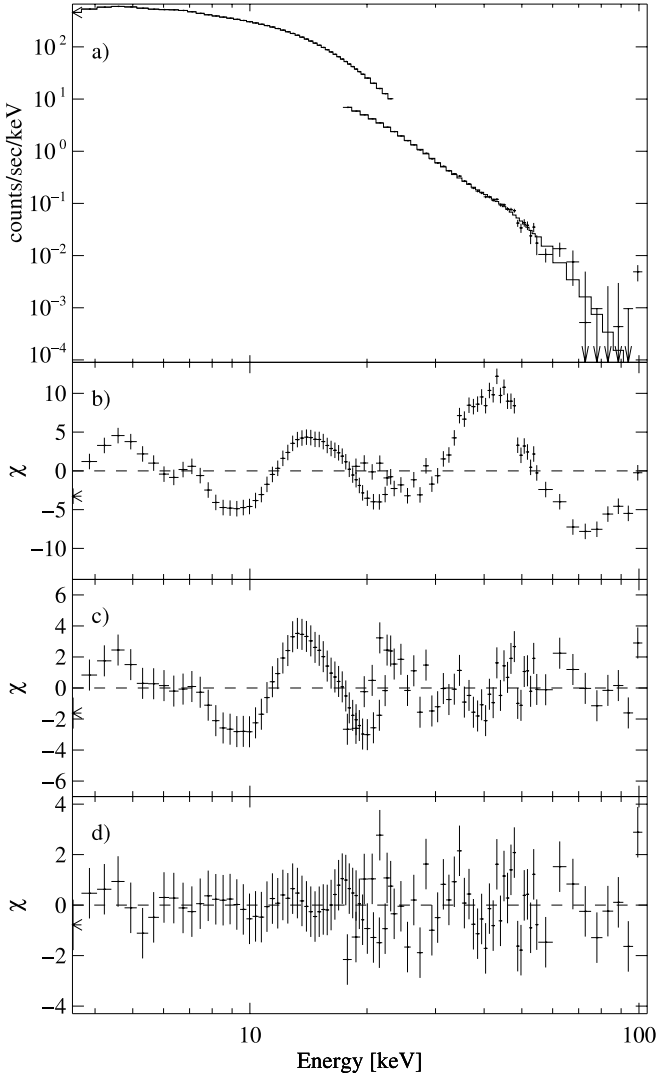


FIG. 2.— (a) PCA and HEXTE phase-averaged counts spectra, accumulated over the first part of the first binary orbit (1A in Fig. 1 and Table 1), and best-fit model. (b) Residuals for an absorbed power law with a Fermi-Dirac cutoff, and a Gaussian Fe line. (c) Improved residuals obtained by adding a cyclotron line at ~ 30 keV. (d) Best-fit residuals obtained by modeling the broad residual around 13 keV with an additional Gaussian emission line. The reduced χ^2 values are 24, 3.4, and 0.97 from (b) to (d). See text for a detailed description of the model components and Table 1 for the best-fit parameters.

a phenomenological model commonly applied to spectra of accreting pulsars (e.g., Kreykenbohm et al. 1999, 2004; Fritz et al. 2006). Figure 2b shows the residuals for fitting an absorbed fdcut model to the averaged broadband spectrum for the first part of orbit 1 (1A in Fig. 1 and Table 1), also including a Gaussian line to model the narrow Fe K emission feature. The reduced χ^2 for this fit is $\chi^2_{\text{red}} = 24$ for 88 degrees of freedom (dof), and an absorption line is clearly visible in the residuals at ~ 25 to 30 keV, which we interpret as a CRSF. To model the CRSF, we used a line shape with a Gaussian optical depth profile that is the basis for past modeling of *RXTE* data (local XSPEC model gauabs). The line is multiplicative with respect to the continuum, leading to the basic spectral model

$$f(E) = F(E) \exp\left(-\frac{\tau_{\text{cyc}}}{2\pi\sigma_{\text{cyc}}} e^{-(1/2)[(E-E_{\text{cyc}})/\sigma_{\text{cyc}}]^2}\right), \quad (3)$$

where $F(E)$ is given by equation (2), and τ_{cyc} , E_{cyc} , and σ_{cyc} are the optical depth, centroid energy, and width of the cyclotron line,

respectively. While including this component improves χ^2_{red} to 3.5 for 86 dof, a strong residual structure remains around ~ 13 keV (Fig. 2c). Adding a single Gaussian emission line at this energy results in a good overall fit, with $\chi^2_{\text{red}} = 1.13$ for 83 dof (Fig. 2d). The same model was also successfully applied to describe the other three time-averaged spectra with the resulting best-fit parameters listed in Table 1. We note that the line parameters do not significantly depend on the continuum model chosen: fits using a negative-positive exponential continuum (local XSPEC model npex; Mihara 1995) instead of the power law with Fermi-Dirac cutoff lead to the same cyclotron line parameters. Compared to a NPEX or hightcut continuum, we achieved slightly better spectral fits using a power law with Fermi-Dirac cutoff. B00 used blackbody emission to describe the spectrum between 0.1 and 2 keV. Our spectral data do not extend below 3.5 keV, and we do not detect any influence of a blackbody at lower energies. Becker & Wolff (2007) are using a Comptonized bremsstrahlung spectrum to calculate the continuum. They state that the contribution of blackbody emission is negligible in their spectrum.

To better understand the observed 13 keV feature, we checked for correlations for all possible pairs of spectral parameters using χ^2 contours. We found no correlation between the parameters characterizing the broad 13 keV feature and the cyclotron line parameters or the rollover of the continuum model. As expected, however, a dependence on the power-law index Γ (and therefore also on N_{H}) was clearly detectable. An increasing Γ or N_{H} value resulted in a lower centroid energy of the 13 keV feature. We conclude that this feature is part of a more complex continuum rather than the simple phenomenological approach used here.

A broad feature at energies below the fundamental cyclotron line, mostly around ~ 10 keV, has also been observed in several other cyclotron line sources, e.g., with *RXTE* in MXB 0656–072 (McBride et al. 2006), Her X-1, 4U 1626–67, 4U 1907+09, and 4U 1538–52 (Coburn et al. 2002), and with *Ginga* in 4U 1538–52, 4U 1907–09, and V0331+53 (Mihara 1995). A weak 10 keV absorption feature was also reported by Santangelo et al. 1998 for a different *BeppoSAX* observation of Cen X-3. Such residuals are usually best described by an additional broad absorption line to improve the fits. In some cases a broad emission line can describe the data better. In our data we find that an emission line at 13 keV describes the observed feature much better. Substituting the 13 keV emission line with a Gaussian absorption line at ~ 8 keV leads to $\chi^2_{\text{red}} = 1.31$ as compared to 1.13 for 83 dof.

As described in § 1, B00 observed quasi-simultaneously with *BeppoSAX* (11 hr overlap with observation 1A from Table 1). A phase-averaged analysis was carried out by these authors using a power law with high-energy cutoff, smoothed around the cutoff energy for the continuum. The CRSF parameters, with $E_{\text{cyc}} = 30.6 \pm 0.6$ keV and $\sigma_{\text{cyc}} = 5.9 \pm 0.7$ keV, are comparable to those presented here. Their measured value of $N_{\text{H}} = (1.95 \pm 0.03) \times 10^{22} \text{ cm}^{-2}$ is still within the error bars of our *RXTE* observation of $N_{\text{H}} = 1.6^{+0.4}_{-0.2} \text{ cm}^{-2}$. Their photon index of $\Gamma = 1.208 \pm 0.007$ is much higher than our value of $\Gamma = 0.92^{+0.06}_{-0.04}$ due to our model definitions. We applied the B00 model to our data and obtained consistent results within error bars. Due to a known deviation in the slope of the Γ -index between *RXTE* PCA and *BeppoSAX* (Kirsch et al. 2005), our resulting value of $\Gamma = 1.26 \pm 0.03$ for the B00 model is marginally consistent.

4.2. Physical Model for CRSF

Ideally, models based on a physical description of the accretion column above the magnetic poles of the neutron star should be used to fit the shape of the cyclotron line and the spectral continuum. Despite recent successes (Becker & Wolff 2007),

however, a fully self-consistent solution to the problem of continuum formation and radiative transfer in neutron star accretion columns is not yet available. Based on earlier work by Araya & Harding (1999) and Araya-Gómez & Harding (2000), we have recently developed a model for the self-consistent determination of cyclotron line profiles (Schönherr et al. 2007) based on a prescribed continuum. Using a Monte Carlo approach and the correct quantum electrodynamical cross sections, Schönherr et al. 2007 calculated the Green's function for the radiative transport for several possible geometries of the accretion column. By convolving an assumed input continuum spectrum with these Green's functions, it is possible to calculate the photon spectrum emerging from the accretion column. The magnetic field is kept constant throughout the accretion column. This approach has been implemented into XSPEC, allowing the direct comparison of the model with observational data. We are presently working on an improved version of the model with magnetic field gradients.

Here we present results from our analysis of the time-averaged 20–70 keV HEXTE data with this model. We limit ourselves to the Green's functions in the 1-0 geometry for the line-forming region (Schönherr et al. 2007; Freeman et al. 1999; Isenberg et al. 1998), where the accretion column is described as a slab with the slab normal being parallel to the magnetic field and the continuum spectrum illuminating the bottom of the slab. This setup mimics a plane-parallel thin emission region close to the surface. The continuum is again taken to be a power law modified by a Fermi-Dirac cutoff (eq. [2]). We decided to exclude N_H from the continuum because it is negligible in the chosen energy range. A gravitational redshift $z = 0.3$ is assumed, a typical value for neutron stars (see § 1). A detailed analysis of several different sources, including phase-resolved analysis, will be presented in a future paper.

Figure 3a shows the residuals after modeling the HEXTE spectrum with the continuum model without taking the cyclotron line formation into account. Introducing the cyclotron line model and refitting significantly reduces the residuals (Fig. 3b), although some structure remains. As has been shown by Schönherr et al. (2007), this structure is caused by the fact that the predicted self-consistent cyclotron line shapes are generally too deep and in addition have significant emission wings, assuming the simplified scenario of a constant magnetic field and simple geometry. These wings are due to so-called spawned photons, which are the result of the stepwise de-excitation of electrons from higher Landau levels after their excitation through a scattering photon (Araya & Harding 1999; Araya-Gómez & Harding 2000). One way of reducing the line depth and strength of the wings is a partial covering approach, where only part of the seed photon spectrum is seen through the accretion column, while the remainder is observed without being modified by the column. Note that this approach is not unique. Other geometries, such as a seed photon source distributed throughout the accretion column, a column with a temperature gradient, or a vertically varying magnetic field, could also result in shallower cyclotron line profiles with less dominant wings (Schönherr et al. 2007).

The result of fitting the data with a partial covering model is shown in Figure 3c. This model describes the data well ($\chi^2_{\text{red}} = 1.35$ for 40 dof). The best-fit parameters are $B = 3.46^{+0.07}_{-0.03} \times 10^{12}$ G for the magnetic field, $kT_e = 7.04^{+0.63}_{-0.48}$ keV for the electron temperature, and $\tau_T = 2.4^{+0.05}_{-0.07} \times 10^{-3}$ for the Thomson optical depth of the continuum, not to be confused with the optical depth of the gauabs model. Note that the optical depth in the lines can be larger by a factor of more than 10^4 (Araya & Harding 1999). The cosine of the angle, θ , between our line of sight and the magnetic field is $\cos \theta = 0.94^{+0.00}_{-0.07}$, i.e., $\theta = 20^{+10}_{-0}$ deg.

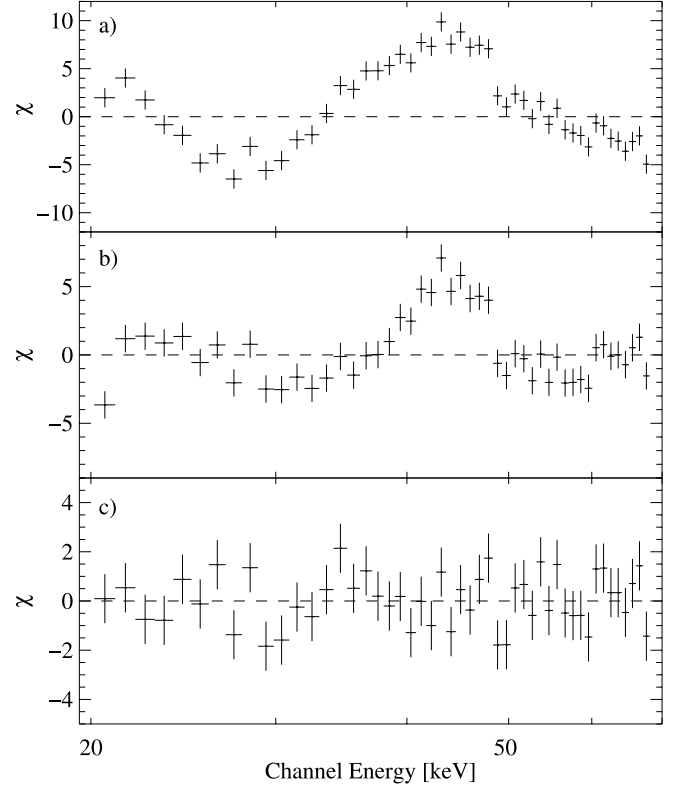


FIG. 3.—Residuals for fitting data with CRSF shapes obtained for Monte Carlo simulations applied on phase-averaged HEXTE data from 20 to 80 keV. (a) Continuum `fdcut*powerlaw` with $\chi^2_{\text{red}} = 24.0$ (45 dof). (b) Included `cyc1omc` model for slab 1-0 geometry showing emission wings ($\chi^2_{\text{red}} = 8.0$ with 41 dof). (c) Added partial covering to reduce emission wings ($\chi^2_{\text{red}} = 1.4$ with 39 dof). Note that the residuals in (a) are slightly different than those shown in Fig. 2a, since only the HEXTE data were modeled.

To check the consistency of our result with that determined in § 4.1, we use the best-fit parameters from above to calculate the centroid energy of the cyclotron line (Schönherr et al. 2007, eq. [3])

$$E_{\text{cyc}} = m_e c^2 \frac{\sqrt{1 + 2B/B_{\text{crit}} \sin^2 \theta} - 1}{\sin^2 \theta} \frac{1}{1 + z}, \quad (4)$$

giving $E_{\text{cyc}} = 30.9^{+0.7}_{-0.3}$ keV for data set 1A. The width of the CRSF can be estimated from Doppler broadening (e.g., Mészáros & Nagel 1985)

$$\Gamma_{\text{FWHM}} = \sqrt{\frac{8(\ln 2)kT_e}{m_e c^2}} \left| \cos \theta \right| E_{\text{cyc}}. \quad (5)$$

In our case we obtain a width of $8.0^{+0.5}_{-0.9}$ keV. Both results lie within the uncertainties of Table 1. The CRSF depth in this model is described by the Thomson optical depth and cannot be directly translated into the gauabs depth due to strong dependencies of the scattering cross section on the emission angle θ .

4.3. Spectral Evolution over the Orbit

This data set allows us to perform the most complete and detailed analysis of the orbital dependence of Cen X-3's broadband spectrum to date. We extracted PCA and HEXTE spectra from the same data modes as for the time-averaged analysis (§ 4.1), but using shorter GTIs, with their duration mainly constrained by

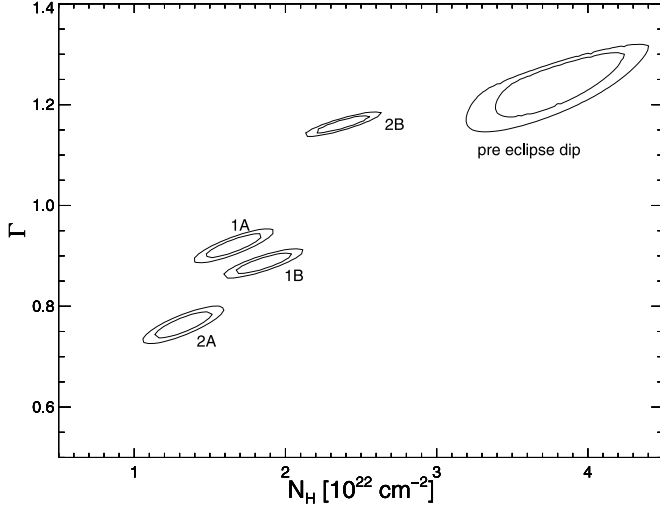


FIG. 4.— χ^2 contours for the four phase-averaged spectra presented in Table 1 and the preeclipse dip. For each data set the 1 and 2 σ confidence levels are shown. Note that the individual N_H - Γ correlation is a nonphysical effect described in the text.

observation gaps due to SAA passages and earth occultations. This selection procedure leads to spectra with a typical exposure time of ~ 3.5 ks ($\Delta\phi_{\text{orb}} \sim 0.03$). Data subsets with considerably longer observation times were further split into subsets of ~ 3.5 ks duration. We ignored data taken during the eclipse, and we also ignored the data set at the end of the preeclipse dip in orbit 1, since no HEXTE data were available. The resulting broadband spectra were then modeled with the same model used to describe the time-averaged spectra in § 4.1. The chosen energy range was 3.5–23 keV for PCA and 18–60 keV for HEXTE.

Figures 1b–1e shows selected time-resolved spectral parameters. As already indicated by the time-averaged results (Table 1), the two orbits show a somewhat different behavior with respect to the two luminosity levels observed in each case. During the first orbit, the parameters are essentially stable within the uncertainties over most of the orbit. N_H increases near eclipse ingress and egress during both orbits (Fig. 1b), as expected from an increasing amount of stellar material in the line of sight (Clark et al. 1988). During the preeclipse dip in orbit 1, N_H is enhanced by a factor of ~ 2 . Γ also increases during the preeclipse dip (Fig. 1c). Error contours for the four phase-averaged observations from § 4.1 and for the preeclipse dip in the first orbit are shown in Figure 4. The observed N_H - Γ correlation for the individual data sets is real and cannot be sufficiently explained by the calculated error contours. This correlation is of unknown origin. The N_H - Γ correlation observed for each individual data set is an artificial effect from the continuum modeling. When modeling the spectrum, one achieves similar χ^2 values for different N_H - Γ combinations, since increasing N_H can compensate for a softer power-law component. Therefore a nonphysical correlation in N_H and Γ is expected.

During the second orbit, we observe a change in the general behavior of many of the spectral parameters that is apparently related to the midorbit luminosity drop. N_H stays relatively constant prior to midorbit and rises continuously afterward (Fig. 1b). Analysis with a frozen Γ value, to take the N_H - Γ correlation into account, showed the same tendency in N_H during the second orbit. As in the preeclipse dip of orbit 1, the power-law Γ slightly increases with N_H (Fig. 1c). The CRSF parameter variability is slightly more pronounced during the second orbit (Figs. 1d–1e).

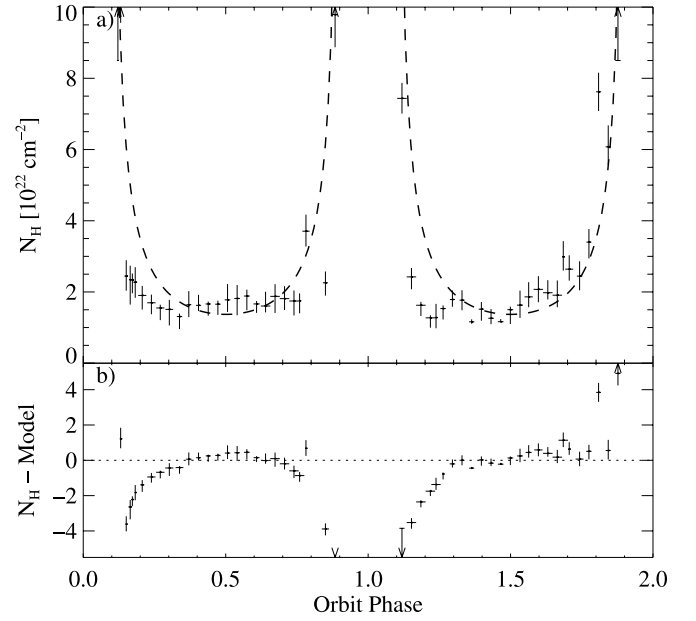


FIG. 5.—(a) Values of N_H as a function of orbital phase (crosses) and calculated model for parameters mentioned in text (dashed line). (b) Difference of N_H and wind model.

Note that the cutoff and folding energies do not show any significant change throughout the whole observation.

4.4. Wind Model

We calculated a simple radiation-driven wind model for N_H , based on the model by Castor et al. (1975, hereafter CAK75), although we note that this assumption of a radiation-driven wind is only an approximation, as it is very likely that the wind is disrupted by the strong X-rays present in the system (Wojdowski et al. 2001, 2003 and references therein). We assumed a mass loss, \dot{m} , for the donor star and the CAK75 velocity profile $v(r) = v_\infty (1 - R_*/r)^\beta$, where v_∞ is the terminal velocity. This gives

$$n_H(r) = \frac{\dot{m}}{4\pi k r^2 v(r)} \quad (6)$$

for the radial particle density profile, where k is a conversion factor from mass to effective proton particle density, assuming a wind with cosmic abundances and a system inclination of 90° and ignoring the orbital eccentricity ($e \leq 0.016$). We then integrate over the density along the line of sight for a specific position in the orbit:

$$N_H = \int_{l_{\text{NS}}}^{\infty} n_H(l') dl', \quad (7)$$

where $l_{\text{NS}} = R_d \cos \phi_{\text{orb}}$ is the position of the neutron star, projected to the celestial plane, where $R_d = 19 R_\odot = 1.58 R_*$ is the separation between neutron star and donor (Blondin 1994). Assuming a typical value of $\beta = 0.8$ (Friend & Abbott 1986), we obtain good results for $\dot{m} = 7 \times 10^{-7} M_\odot \text{ yr}^{-1}$ and $v_\infty = 1200 \text{ km s}^{-1}$ (Fig. 5a). For better comparison, we also show the difference between data and model (Fig. 5b). Due to the definition of the model, a strong correlation between increasing mass loss and terminal velocity is present, such that absolute values cannot be determined by this approach.

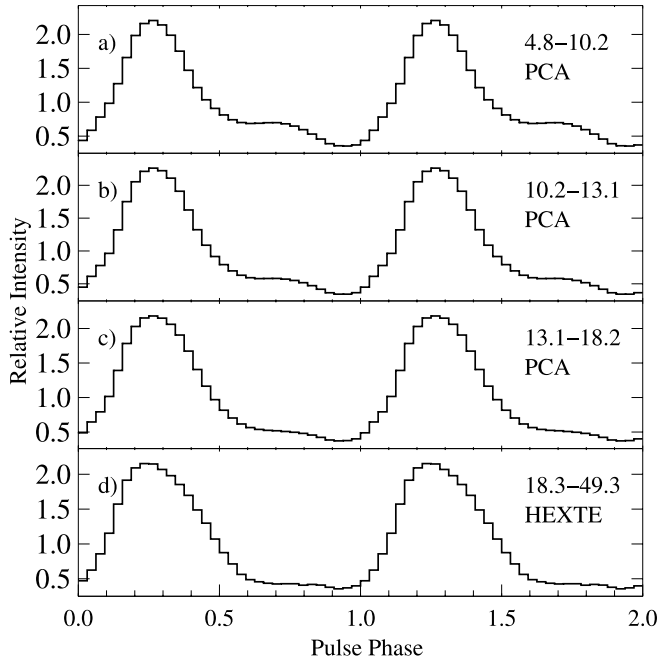


FIG. 6.—Normalized PCA and HEXTE pulse profiles for four energy bands: (a) 4.8–10.2 keV, (b) 10.2–13.1 keV, (c) 13.1–18.2 keV, and (d) 18.3–49.3 keV. A secondary peak at pulse phase ~ 0.7 is visible for lower energies.

Both orbits show a different behavior in the evolution of N_H . During the first orbit, where N_H is mostly constant, we see a symmetrical deviation during eclipse ingress and egress, when our simple approach fails to model the data. A similar deviation is seen at the beginning of the second orbit. After midorbit, N_H keeps increasing for the remainder of the orbit, indicating an increased absorption in the second half of the orbit. A similar behavior has been simulated by Blondin et al. (1990) and probably indicates the presence of an accretion wake in this system. A small bump around $\phi_{\text{orb}} = 0.3$ – 0.4 can be observed in both orbits, more pronounced in the second one. This bump also exists in the simulation and is another indication of a tidal wake.

5. PHASE-RESOLVED SPECTROSCOPY

5.1. Pulse Profile

Pulse profiles with 32 phase bins for four energy bands were extracted for each of the 12 ObsIDs. We decided to use locally determined pulse periods for each ObsID and the ephemeris from Nagase et al. (1992) after using the ephemeris and period from B00 did not result in consistent pulse profiles. All pulse profiles showed a similar shape, with a main peak at pulse phase (ϕ_{pulse}) ~ 0.3 , which allowed us to combine them after phase alignment. Figure 6 shows the resulting pulse profiles for four different energy ranges. A second weak peak at pulse phase of ~ 0.7 is visible at energies below 18 keV. Nagase et al. (1992) observed Cen X-3 in 1989 March with *Ginga* when the source had a 1–37 keV luminosity of 5×10^{37} ergs s $^{-1}$, a factor of 2 fainter than during this *RXTE* observation, and presents pulse profiles for nine energy bands. At lower energies, they observe a double-peaked profile, where both peaks have equal intensities below 7 keV. Above 18 keV, the profile is comparable to our results, with only one main peak. Audley et al. (2001) showed that the 2–25 keV pulse profile is highly variable, changing between an asymmetric double-peaked pulse profile, as in our observation, and a much more complex pulse profile with multiple peaks, depending on the count rate of the binary system.

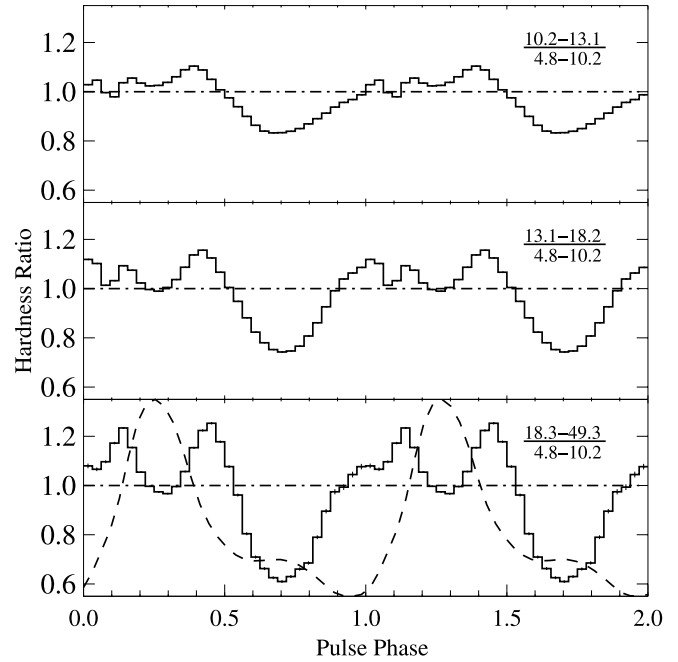


FIG. 7.—Normalized hardness ratios. Each panel has been calculated by taking the corresponding pulse profile from Fig. 6 divided by panel (a) from Fig. 6. The pulse profile is indicated in the bottom panel (dashed line). The top right corner of each panel shows the energy ranges.

We used the pulse profiles presented in Figure 6 to create hardness ratios for each energy band using the lowest energy range as a baseline (Fig. 7). At $\phi_{\text{pulse}} = 0.7$, we see the decrease in hardness of the secondary peak toward higher energies. The rise and decay of the main peak ($\phi_{\text{pulse}} = 0.1$ and 0.5) show peaks in the hardness ratio, a clear indication that the lower energy emission region is beamed more sharply. It is not clear whether a third peak, visible at $\phi_{\text{pulse}} = 1.0$, originates from a real physical feature or is part of an artificial wing from a phase continuity in the plot.

5.2. Spectral Evolution over the Pulse Profile

Extraction of phase-resolved spectra for each individual ObsID with 32 phase bins resulted in large uncertainties for the individual parameters. We therefore created phase-resolved spectra for each ObsID with eight phase bins and observed similarities in the behavior of the spectral parameters, e.g., an increase of the CRSF centroid energy during the rise of the main peak. We decided to sum all ObsIDs and use 32 phase bins, resulting in an integration time of ~ 12 ks for a phase analysis. In the pulse minimum, we binned the phases by a factor of 2, and even by a factor of 6 for the secondary peak, to be able to constrain the CRSF feature. This results in a total of 24 phase bins, on which we performed a spectral analysis using the model defined in § 4.1. Figure 8 shows the best-fit values of selected parameters over the pulse period. Compared to the phase-averaged analysis, not only N_H and Γ , but also the CRSF parameters, change drastically over the pulse period.

The pulse profile can be roughly divided into three regions where the continuum parameters are significantly different, main peak, secondary peak, and pulse minimum. The column density N_H is constant, with a value of $1.5^{+0.3}_{-0.4} \times 10^{22}$ cm $^{-2}$ during the main peak. Between the main and secondary peaks, this value suddenly jumps up, to $2.2^{+0.2}_{-0.3} \times 10^{22}$ cm $^{-2}$. The χ^2 contours indicate that this increase is not due to statistical fluctuations. During the pulse minimum, the N_H value reaches a minimum of

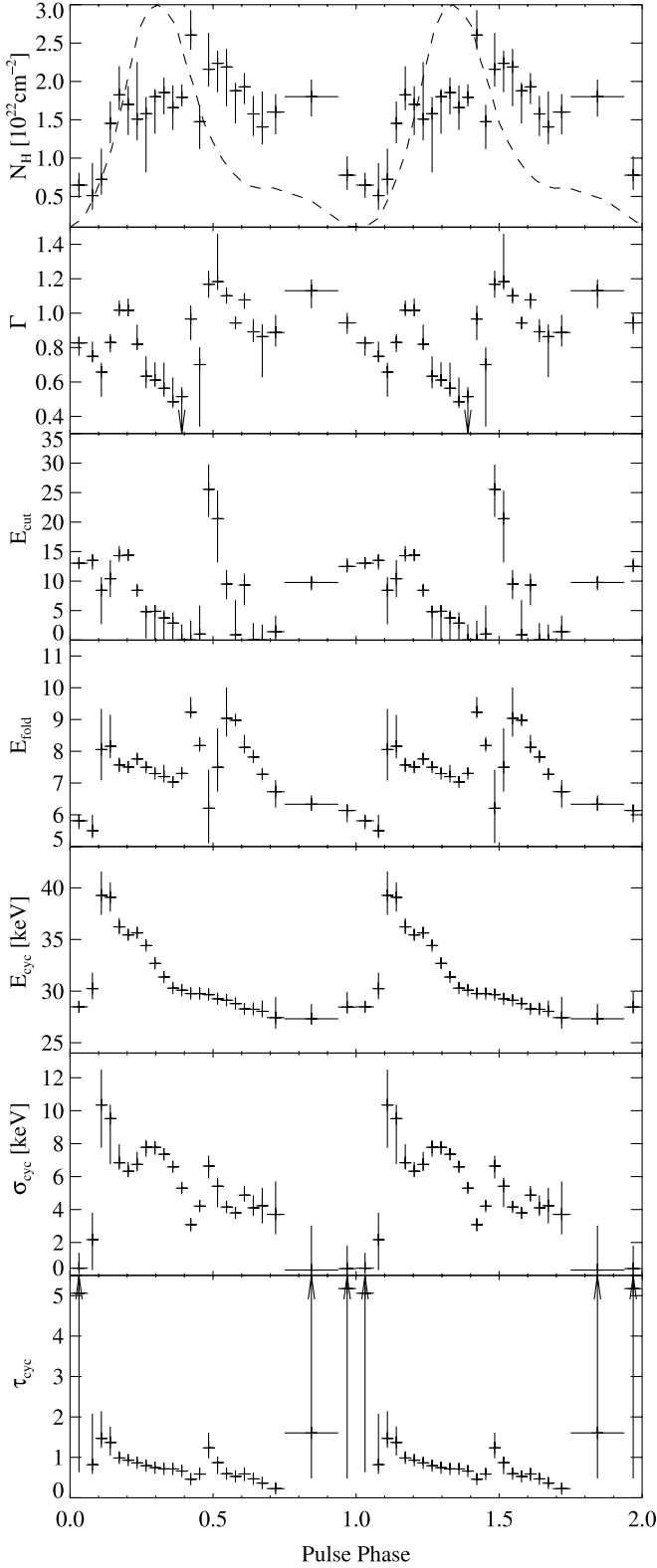


FIG. 8.— Selected spectral parameters over the pulse profile (*dotted line*). The last phase bins are binned. Error bars indicate 1σ deviations.

$0.5^{+0.5}_{-0.2} \times 10^{22} \text{ cm}^{-2}$. Another interpretation would be that N_H follows the shape of the pulse profile and is somehow capped during the main peak. We have not identified a physical explanation for this observational fact, which might be caused by the limitations of the current continuum modeling. The power-law

index Γ also changes strongly over the pulse phase. It increases during the rise of the pulse up to a value of $1.0^{+0.1}_{-0.1}$ and then decreases to $0.5^{+0.2}_{-0.3}$ for the duration of the main peak. After the main peak, the value jumps back up to $1.2^{+0.1}_{-0.1}$. The CRSF centroid energy also shows a drastic change throughout the pulse. During the rise of the main peak, the value increases from ~ 30 keV to almost 40 keV, slowly decreasing throughout the main peak and descending below the phase average value of less than 30 keV. The evolution of the CRSF throughout the pulse is similar to the shape of the pulse profile, with a phase shift of $\Delta\phi_{\text{pulse}} = 0.2$ (ignoring the two outliers in the pulse rise, we still obtain $\Delta\phi_{\text{pulse}} = 0.1$). The width σ_{cyc} of the CRSF approximately follows the evolution of the centroid energy over the main peak and drops to ~ 0 during the off-pulse, an indication that the CRSF is not well constrained. The depth τ_{cyc} is slowly decreasing throughout the whole pulse and is also much less constrained during the pulse minimum. Compared to the other known sources featuring a variation of the CRSF, e.g., Her X-1 (Gruber et al. 2001), Vela X-1 (La Barbera et al. 2003; Kreykenbohm et al. 2002), 4U 0352+309 (Coburn et al. 2001), and GX 301–2 (Kreykenbohm et al. 2004), Cen X-3 is the only known source to show an increase in centroid energy during the ascent of the main pulse.

B00 also provided a phase-resolved analysis, but they divided the pulse into only four parts: ascent, maximum, descent of the main peak, and minimum, including the secondary peak. They also observe an increase in the CRSF centroid energy up to $36.6^{+1.6}_{-2.4}$ keV in the ascent. We combined the phase-resolved spectra according to the phase bins in B00 and applied their model to our results. We can confirm the results from B00 within the error bars with small deviations for Γ .

6. DISCUSSION AND CONCLUSIONS

In this paper we presented the data analysis of the HMXB Cen X-3 observed for two consecutive orbits. We conducted phase-averaged analysis for different parts of the orbit, distinguished by a drop in the overall count rate. A decrease in the 2–10 keV luminosity between the first and second orbit by $\sim 20\%$ can be observed and could be caused by a decrease in the overall amount of matter accreted onto the neutron star. In addition, pulse phase-resolved spectroscopy was performed. Here the long duration of the observations allowed us to study the pulse phase dependence of the cyclotron line parameters in unprecedented detail. In the following two sections, we summarize the major results of these two studies, starting with the orbital variability of the X-ray spectrum.

6.1. Orbital Variability of the X-Ray Spectrum

The analysis for individual satellite orbits shows the evolution of the spectral parameters throughout both orbits. We see a difference between both orbits, not only in the luminosity, but also in the evolution of N_H and Γ , which are correlated to each other. Comparison with a simple CAK75 wind model showed that, while reproducing the overall trends in N_H , such a model is not sufficient to describe the observed data fully, regardless of inaccuracies during eclipse ingress and egress. Wojdowski et al. (2001) use a similar approach on a Cen X-3 data set from the *Advanced Satellite for Cosmology and Astrophysics (ASCA)* with significantly different results. Probing the parameter space, they find best-fit values for $\beta = 0.57^{+0.06}_{-0.07}$ and

$$\Xi = \frac{\dot{M}}{10^{-6} M_{\odot} \text{ yr}^{-1}} \left(\frac{v_{\infty}}{1000 \text{ km s}^{-1}} \right)^{-1} \left(\frac{d}{10 \text{ kpc}} \right)^{-1} \quad (8)$$

with $\Xi = 1.56$. Applying these parameters to our model, we find a minimum N_{H} value of $3.2 \times 10^{22} \text{ cm}^{-2}$, 1.5 times higher than our observed data. Also the change of N_{H} during ingress and egress of the eclipse is not as drastic as observed here. With a fixed $\beta = 0.8$ and $\Xi = 0.7$, we obtain the results shown in Figure 5.

In our data set a small increase in N_{H} is seen in the first half ($\phi_{\text{orb}} = 0.3\text{--}0.4$) in both orbits, more pronounced in the second orbit. Blondin et al. 1991 used two-dimensional numerical simulations based on the CAK75 model to calculate the column density in massive X-ray binary systems with a tidal stream and observes such an increase in N_{H} around $\phi_{\text{orb}} = 0.4\text{--}0.5$. They interpret this as a leading bow shock in front of the accretion stream that is extremely sensitive to orbital parameters, e.g., the distance between neutron star and donor or the intensity of the stellar wind. A possible explanation of our observed increase is that it corresponds to this bow shock observed in the simulations. In the second half of the orbit, Blondin et al. (1991) see a general increase in N_{H} , comparable to our observations during the second orbit. This increase could be due to material in the line of sight, trailing the tidal wake. Taking into account that the continuum parameters do not change significantly over the orbit, we can rule out that the system changed its state. Similar increases have been observed in other sources, e.g., 4U 1700–37 (Haberl et al. 1989) and Vela X-1 (Haberl & White 1990); both systems are believed to have tidal streams. In these cases, the difference was more than an order of magnitude, whereas here the increase is on the order of a factor of 2–3. We point out that we also observe a change in N_{H} with a fixed photon index, so that the $N_{\text{H}}\text{--}\Gamma$ correlation alone cannot be responsible for this rise. The fact that this increase is visible only during the second orbit could imply that the overall luminosity has an influence on the visibility of the accretion wake.

We do not rule out other possible explanations for the differences in orbit 1 and 2. Blondin et al. (1990) showed in their simulations that the column density throughout the orbit changes between consecutive orbits due to variability in the accretion flow. The drop in luminosity of $\sim 20\%$ between orbit 1 and 2 indicates the decrease of \dot{m} . In the simulations Blondin et al. (1991) observe instabilities for lower luminosities, i.e., less photon pressure from the donor star, trailing the tidal wake. These instabilities can create small pockets of denser material, which also could be responsible for the observed increase in N_{H} .

Another hint for the existence of multiple material clumps is seen in the light curve. Compared to the first orbit, the second orbit shows multiple preeclipse dips. In the first orbit, during the preeclipse dip, N_{H} increases by a factor of ~ 2 . Multiple dips close together could cause an overall increase of N_{H} throughout the second orbit. One small drawback to this theory is that the increase in N_{H} starts directly after the midorbit break, whereas the preeclipse dips are occurring at $\phi_{\text{orb}} > 0.7$ of the second orbit. Therefore we do not think that preeclipse dips can be exclusively responsible for the rise.

6.2. Spectral and Pulse Phase Variability

We divided each orbit into two parts, before and after mid-orbit break, and extracted phase-averaged spectra for each part. For the analysis we applied a power law with a Fermi-Dirac cut-off as continuum with an additional iron emission line. A CRSF at $\sim 30 \text{ keV}$ is visible in all data sets, consistent with previous observations. The widely used local model *gauabs* gave us best-fit results for this feature. No significant changes in the spectral parameters could be observed throughout the orbit. An additional broad Gaussian emission feature at 13 keV had to be

introduced to get reasonable residuals. We checked for correlations of this feature with other model parameters and determined that it is probably an artifact of the current continuum modeling. We conclude that the 13 keV feature corresponds to the 10 keV absorption feature that has been observed in multiple different sources and with different instruments. Further investigation of this feature is necessary, but this is beyond the scope of this paper.

We also applied a newly developed physical model, *cyclomc* (Schönherr et al. 2007), based on Monte Carlo simulations, to part of the phase-averaged data (data set 1A). This model is self-consistent in determining the CRSF parameters using the Green's function for radiative transport. For all geometries of the line-forming region available in the current implementation of the model, we generally find that the predicted CRSFs are too deep and possess significant emission wings, leading to difficulties when matching the observed spectra. The slab 1-0 geometry, where the continuum is illuminating the bottom of the accretion column, has the smallest emission wings of the geometries tested and is therefore a good candidate for a first approach. Assuming partial covering of the continuum leads to a further reduction of the remaining emission wings. This approach is motivated by the idea that only part of the continuum contribution emerges from the line-forming region. The results are encouraging and in good agreement with the previous phenomenological approach. It is planned to improve this model by, e.g., adding magnetic fields that are gradually changing over the accretion column and applying it to different sources with known CRSFs as part of a future paper.

For the phase-resolved analysis, we created pulse profiles in different energy bands over the whole observation. They show a main peak and a much smaller secondary peak, which is seen only at lower energies. Compared to other sources, e.g., Vela X-1 or GX 301–2, the pulse profile is rather smooth and does not show a complex shape at lower energies. The main peak is more pronounced at lower energies and slightly asymmetric, steeper in the rise, at higher energies. Comparing with Nagase et al. (1992), where a clear double-peaked profile at lower energies has been observed, we assume that this is a luminosity-dependent effect on the pulse profile. During the observation of Nagase et al. (1992), Cen X-3 was fainter than during our second orbit, and no changes in the pulse profiles have been observed throughout our observation.

For each bin in the pulse profile, we extracted a spectrum to study the evolution of the parameters over the pulse. For better statistics, we combined some of the data in the pulse minimum, resulting in 24 phase bins overall. The continuum parameters show some significant changes throughout the pulse, and the general $N_{\text{H}}\text{--}\Gamma$ correlation seems not to be valid during the main peak.

The CRSF shows significant changes throughout the pulse. The shape of the changes is very similar to the pulse profile shifted by $\Delta\phi_{\text{pulse}} = 0.1$, not including the two maximum values during the rise. These outliers have rather large uncertainties and should be handled with caution in the interpretation. From the main peak on, E_{cyc} slowly decreases to below 30 keV , where it stays for the remainder of the pulse. Figure 9 shows how the magnetic field deduced from these measurements varies as a function of pulse phase. The figure also shows the earlier *BeppoSAX* measurements of B00, which are consistent with our much finer resolved data.

B00 argued that the large variation in B -field with pulse phase could not be due to a variation of the height in the accretion column at which the observed radiation originates, since this

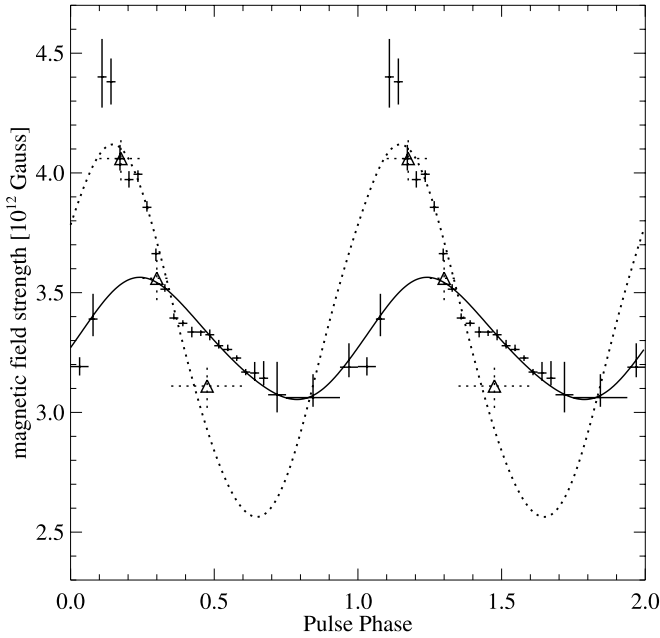


FIG. 9.— Calculated magnetic field strengths (*crosses*) and B00 results (*triangles*) using the CRSF centroid energy. The dotted line shows the single-dipole model using parameters from B00. The solid line shows the best fit of the single-dipole model to our data. [See the electronic edition of the *Journal* for a color version of this figure.]

variation would imply height differences of kilometers. B00 instead argue that, based on earlier studies of the pulse shape of Cen X-3 by Leahy (1991), the polar cap of Cen X-3 is rather large. If this assumption is true, then it is likely that different locations on the neutron star's surface are observed over one rotation of the neutron star. Using the assumption that the observed X-rays are produced by only one of the two magnetic poles and that the observed X-rays are all coming from a location at a constant geographical colatitude of the neutron star (taken by B00 to be the system's inclination), B00 then show that the variation of the B -field at the neutron star's surface produced by a magnetic dipole offset by $0.1 R_{\text{NS}}$ from the rotational axis of the neutron star can explain the B -field variation seen by *BeppoSAX*. We reproduce their best-fit model in Figure 9. While the model is sufficient to explain the *BeppoSAX* data, the higher resolution *RXTE* data clearly show that it is not a viable explanation for the observed B -field variation. We extended the approach of B00 by allowing for observations of both magnetic poles and also removing the constraint that the colatitude at which the X-rays originate equals the inclination. Neither

of these approaches resulted in statistically satisfying descriptions of the variation of B with ϕ_{pulse} . Even when relaxing the model assumptions further, by using a skew-symmetric magnetic dipole, which approximates higher multipole moments for the B -field on the surface, and assuming that the X-rays come from two different locations on the neutron star, no satisfying description of the observed line variation was found. We therefore conclude that the model of B00 is not a viable description of the high-resolution B -field variation seen here.

We note that an alternative study of the pulse profile of Cen X-3 has been presented by Kraus et al. (1996). Similar to the assumptions outlined above, these authors show that the shape and energy dependence of the pulse profile can be explained by emission from a distorted magnetic dipole. Taking into account the relativistic photon propagation close to the neutron star, Kraus et al. (1996) show that, in order to explain the pulse profile, both magnetic poles must contribute to the observed emission. Modeling observations of Cen X-3 made at a luminosity state similar to the one during the *RXTE* observation, Kraus et al. (1996) show that these assumptions yield an offset of approximately 10° for both poles and that both poles contribute equally to the observed flux. In these models, they assume that the polar caps' radiation characteristic is a pen+pencil-beam pattern. A major result of these models is that in this decomposition the main pulse emission is dominated by the magnetic pole facing toward the observer, while the wings of the main pulse are dominated by the pole facing away from the observer. Although they do not take the height of the accretion column into account, we believe it is likely that for geometric reasons the X-rays observed from the magnetic pole on the neutron star hemisphere facing away from the observer originate at a distance farther away from the neutron star surface, thus in a region of lower B -field. Together with the possibility of slightly different surface magnetic strengths at both poles, we therefore deem it likely that the observed B -field variation over the X-ray pulse is due to us observing the two accretion columns at different heights, although further modeling of such a geometric setup is clearly required before a final answer about the origin of the B -field variation can be given.

We acknowledge the support of NASA contract NAS5-30720, DLR contract 50OR0302, a travel grant from the Deutscher Akademischer Austauschdienst, and support provided by the Studienstiftung des Deutschen Volkes to V. G. and G. S. We thank the members of the pulsar team supported by the International Space Science Institute (ISSI) in Bern, Switzerland, for discussions that greatly helped shape the ideas presented in this paper, and ISSI itself for its hospitality.

REFERENCES

- Araya, R. A., & Harding, A. K. 1999, *ApJ*, 517, 334
 Araya-Gómez, R. A., & Harding, A. K. 2000, *ApJ*, 544, 1067
 Arnaud, K. A. 1996, in *ASP Conf. Ser. 101, Astronomical Data Analysis Software and Systems V*, ed. G. H. Jacoby & J. Barnes (San Francisco: ASP), 17
 Ash, T. D. C., Reynolds, A. P., Roche, P., Norton, A. J., Still, M. D., & Morales-Rueda, L. 1999, *MNRAS*, 307, 357
 Audley, M. D., Nagase, F., Kelley, R. L., & Vrtilek, S. D. 2001, in *ASP Conf. Ser. 251, New Century of X-Ray Astronomy*, ed. H. Inoue & H. Kunieda (San Francisco: ASP), 336
 Becker, P. A., & Wolff, M. T. 2007, *ApJ*, 654, 435
 Bildsten, L., et al. 1997, *ApJS*, 113, 367
 Blondin, J. M. 1994, *ApJ*, 435, 756
 Blondin, J. M., Kallman, T. R., Fryxell, B. A., & Taam, R. E. 1990, *ApJ*, 356, 591
 Blondin, J. M., Stevens, I. R., & Kallman, T. R. 1991, *ApJ*, 371, 684
 Burderi, L., Di Salvo, T., Robba, N. R., La Barbera, A., & Guainazzi, M. 2000, *ApJ*, 530, 429 (B00)
 Canuto, V., & Ventura, J. 1977, *Fundam. Cosmic Phys.*, 2, 203
 Castor, J. I., Abbott, D. C., & Klein, R. I. 1975, *ApJ*, 195, 157 (CAK)
 Clark, G. W., Minato, J. R., & Mi, G. 1988, *ApJ*, 324, 974
 Clark, G. W., Woo, J. W., Nagase, F., Makishima, K., & Sakao, T. 1990, *ApJ*, 353, 274
 Coburn, W., Heindl, W. A., Gruber, D. E., Rothschild, R. E., Staubert, R., Wilms, J., & Kreykenbohm, I. 2001, *ApJ*, 552, 738
 Coburn, W., Heindl, W. A., Rothschild, R. E., Gruber, D. E., Kreykenbohm, I., Wilms, J., Kretschmar, P., & Staubert, R. 2002, *ApJ*, 580, 394
 Day, C. S. R., Nagase, F., Asai, K., & Takeshima, T. 1993, *ApJ*, 408, 656
 Day, C. S. R., & Tennant, A. F. 1991, *MNRAS*, 251, 76
 Freeman, P. E., Lamb, D. Q., Wang, J. C. L., Wasserman, I., Lored, T. J., Fenimore, E. E., Murakami, T., & Yoshida, A. 1999, *ApJ*, 524, 772
 Friend, D. B., & Abbott, D. C. 1986, *ApJ*, 311, 701

- Fritz, S., Kreykenbohm, I., Wilms, J., Staubert, R., Bayazit, F., Pottschmidt, K., Rodriguez, J., & Santangelo, A. 2006, *A&A*, 458, 885
- Giacconi, R., Gursky, H., Kellogg, E., Schreier, E., & Tananbaum, H. 1971, *ApJ*, 167, L67
- Gruber, D. E., Heindl, W. A., Rothschild, R. E., Coburn, W., Staubert, R., Kreykenbohm, I., & Wilms, J. 2001, *ApJ*, 562, 499
- Haberl, F., & White, N. E. 1990, *ApJ*, 361, 225
- Haberl, F., White, N. E., & Kallman, T. R. 1989, *ApJ*, 343, 409
- Heindl, W. A., & Chakrabarty, D. 1999, in *Highlights in X-Ray Astronomy*, ed. B. Aschenbach & M. J. Freyberg (MPE Rep. 272; Garching: MPE), 25
- Hutchings, J. B., Cowley, A. P., Crampton, D., van Paradijs, J., & White, N. E. 1979, *ApJ*, 229, 1079
- Isenberg, M., Lamb, D. Q., & Wang, J. C. L. 1998, *ApJ*, 505, 688
- Jahoda, K., Markwardt, C. B., Radeva, Y., Rots, A. H., Stark, M. J., Swank, J. H., Strohmayer, T. E., & Zhang, W. 2006, *ApJS*, 163, 401
- Kirsch, M. G., et al. 2005, *Proc. SPIE*, 5898, 22
- Kohmura, T., Kitamoto, S., & Torii, K. 2001, *ApJ*, 562, 943
- Kraus, U., Blum, S., Schulte, J., Ruder, H., & Mészáros, P. 1996, *ApJ*, 467, 794
- Kreykenbohm, I., Coburn, W., Wilms, J., Kretschmar, P., Staubert, R., Heindl, W. A., & Rothschild, R. E. 2002, *A&A*, 395, 129
- Kreykenbohm, I., Kretschmar, P., Wilms, J., Staubert, R., Kendziorra, E., Gruber, D. E., Heindl, W. A., & Rothschild, R. E. 1999, *A&A*, 341, 141
- Kreykenbohm, I., Wilms, J., Coburn, W., Kuster, M., Rothschild, R. E., Heindl, W. A., Kretschmar, P., & Staubert, R. 2004, *A&A*, 427, 975
- Krzeminski, W. 1974, *ApJ*, 192, L135
- La Barbera, A., Santangelo, A., Orlandini, M., & Segreto, A. 2003, *A&A*, 400, 993
- La Barbera, A., Segreto, A., Santangelo, A., Kreykenbohm, I., & Orlandini, M. 2005, *A&A*, 438, 617
- Leahy, D. A. 1991, *MNRAS*, 251, 203
- . 2002, *A&A*, 391, 219
- Leahy, D. A., & Kostka, M. 2008, *MNRAS*, 384, 747
- McBride, V. A., et al. 2006, *A&A*, 451, 267
- Mészáros, P., & Nagel, W. 1985, *ApJ*, 298, 147
- Mihara, T. 1995, Ph.D. thesis, Univ. of Tokyo
- Mowlavi, N., et al. 2006, *A&A*, 451, 187
- Nagase, F., Corbet, R. H. D., Day, C. S. R., Inoue, H., Takeshima, T., Yoshida, K., & Mihara, T. 1992, *ApJ*, 396, 147
- Nakajima, M., Mihara, T., Makishima, K., & Niko, H. 2006, *ApJ*, 646, 1125
- Nishimura, O. 2005, *PASJ*, 57, 769
- Pettersson, J. A. 1978, *ApJ*, 224, 625
- Pottschmidt, K., et al. 2005, *ApJ*, 634, L97
- Rothschild, R. E., et al. 1998, *ApJ*, 496, 538
- . 2006, *ApJ*, 641, 801
- Santangelo, A., del Sordo, S., Segreto, A., dal Fiume, D., Orlandini, M., & Piraino, S. 1998, *A&A*, 340, L55
- Schönherr, G., Wilms, J., Kretschmar, P., Kreykenbohm, I., Santangelo, A., Rothschild, R. E., Staubert, R., & Coburn, W. 2007, *A&A*, 472, 353
- Schreier, E., Levinson, R., Gursky, H., Kellogg, E., Tananbaum, H., & Giacconi, R. 1972, *ApJ*, 172, L79
- Soong, Y., Gruber, D. E., Peterson, L. E., & Rothschild, R. E. 1990, *ApJ*, 348, 641
- Staubert, R., Shakura, N. I., Postnov, K., Wilms, J., Rothschild, R. E., Coburn, W., Rodina, L., & Klochkov, D. 2007, *A&A*, 465, L25
- Stevens, I. R. 1988, *MNRAS*, 232, 199
- Takeshima, T., Dotani, T., Mitsuda, K., & Nagase, F. 1991, *PASJ*, 43, L43
- Tanaka, Y. 1986, in *IAU Colloq. 89, Radiation Hydrodynamics in Stars and Compact Objects*, ed. D. Mihalas & K.-H. A. Winkler (Heidelberg: Springer), 198
- Tjemkes, S. A., van Paradijs, J., & Zuiderwijk, E. J. 1986, *A&A*, 154, 77
- Tsunemi, H., Kitamoto, S., & Tamura, K. 1996, *ApJ*, 456, 316
- Wojdowski, P. S., Liedahl, D. A., & Sako, M. 2001, *ApJ*, 547, 973
- Wojdowski, P. S., Liedahl, D. A., Sako, M., Kahn, S. M., & Paerels, F. 2003, *ApJ*, 582, 959